ARMY RESEARCH LABORATORY

Fabrication and Testing of a Novel MEMS Rotational Thermal Actuator

by Danny Gee and Luke Currano

ARL-TR-4315 **November 2007**

NOTICES

Disclaimers

The findings in this report are not to be construed as an official Department of the Army position unless so designated by other authorized documents.

Citation of manufacturer's or trade names does not constitute an official endorsement or approval of the use thereof.

Destroy this report when it is no longer needed. Do not return it to the originator.

Army Research Laboratory
Adelphi, MD 20783-1197

ARL-TR-4315 **November 2007**

Fabrication and Testing of a Novel MEMS Rotational Thermal Actuator

Danny Gee and Luke Currano
Sensors and Electron Devices Directorate, ARL

REPORT DOCUMENTATION PAGE

Form Approved
OMB No. 0704-0188

1. REPORT DATE *(DD-MM-YYYY)*	**2. REPORT TYPE**	**3. DATES COVERED (From - To)**
November 2007	Final	May to August 2007

4. TITLE AND SUBTITLE
Fabrication and Testing of a Novel MEMS Rotational Thermal Actuator

5a. CONTRACT NUMBER

5b. GRANT NUMBER

5c. PROGRAM ELEMENT NUMBER

6. AUTHOR(S)
Danny Gee and Luke Currano

5d. PROJECT NUMBER

5e. TASK NUMBER

5f. WORK UNIT NUMBER

7. PERFORMING ORGANIZATION NAME(S) AND ADDRESS(ES)
U.S. Army Research Laboratory
ATTN: AMSRD-ARL-SE-RL
2800 Powder Mill Road
Adelphi, MD 20783-1128

8. PERFORMING ORGANIZATION REPORT NUMBER
ARL-TR-4315

9. SPONSORING/MONITORING AGENCY NAME(S) AND ADDRESS(ES)
U.S. Army Research Laboratory
2800 Powder Mill Road
Adelphi, MD 20783-1128

10. SPONSOR/MONITOR'S ACRONYM(S)

11. SPONSOR/MONITOR'S REPORT NUMBER(S)

12. DISTRIBUTION/AVAILABILITY STATEMENT
Approved for public release; distribution unlimited.

13. SUPPLEMENTARY NOTES

14. ABSTRACT
The fabrication and testing of a micromachined thermal rotational actuator are presented in this report. The actuator is designed to realize the high forces and large displacements that are difficult to achieve with microelectromechanical system actuators. The device uses asymmetry to produce a desired rotational deflection, making it well suited for rotary engines or biologically inspired joint movement. The focus of the project was to compare measured and theoretical values of spring constants of the devices, since spring constant relates force and displacement. These measurements both characterize actuator performance for comparisons with other actuators and provide a basis for optimal design of this type of actuator for any given application. An early test of the rotational actuators showed a displacement of 12.7 μm with 637 milliNewtons (mN) of force requiring 250 mW of power.

15. SUBJECT TERMS
MEMS, thermal actuator, rotation, torsion, offset beam

16. Security Classification of:			**17. LIMITATION OF ABSTRACT**	**18. NUMBER OF PAGES**	**19a. NAME OF RESPONSIBLE PERSON**
a. REPORT	**b. ABSTRACT**	**c. THIS PAGE**			Danny Gee
U	U	U	U	22	**19b. TELEPHONE NUMBER** (*Include area code*) (301) 394-1277

Standard Form 298 (Rev. 8/98)
Prescribed by ANSI Std. Z39.18

Contents

List of Figures

List of Tables

1. Introduction

Historically, microelectromechanical system (MEMS) actuators have relied on simplified designs, focusing on in-plane, one-dimensional, linear deflections. However, as the microsystems industry continues to mature, more complex systems are requiring large displacement, high-force actuators with smaller chip size constraints, which cannot be achieved by the limitations of previous designs. The proposed rotational electrothermal actuator is a candidate for these applications, achieving maximum lateral displacements of 23 μm with near millinewton forces.

The performance of a MEMS actuator is highly related to its method of actuation. Electrostatic actuators are simple in design and are easily integrated into circuits but require very high voltages (*1*). Conversely, magnetic actuators require high currents and are inefficient in thin film form (*2*). Piezoelectrics are efficient and have high energy densities; however, they are difficult to design for in-plane movement and integration with complementary metal oxide semiconductor processing (*3*). Thermal actuators are typically regarded as inefficient while yielding high forces and small displacements or high displacements and small forces. The proposed device is intended to compensate for the disadvantages of thermal actuators and to effectively yield medium displacements and medium forces.

This thermal actuator was designed by Luke Currano of the U.S. Army Research Laboratory, with the intention of resetting latching MEMS sensors and powering micro-gears for locomotive devices (*4*). Rotational deflections of 28 μm while pushing a cantilever with a linear spring constant of about 65.5 N/m have been achieved at 39 mA and 13.3 V. There is also current work in the design and fabrication of an in-plane piezoelectric actuator, which should demonstrate improved electrical efficiency with similar displacements and forces.

This report examines the theory and fabrication process of the actuators and reports measured performance for a few particular designs. Since the primary interest is in the performance relationship between actuation force and linear displacement, the spring constants and power consumption of the devices are investigated.

2. Experiment

2.1 Theory

The rotational actuator consists of three beams connected at a common yoke, as shown in figure 1. The two actuating beams are parallel, yet offset each other and are fixed at opposite ends, and the third beam is free to deflect. When a current is applied to the thermal actuator, the

actuator beams heat, causing the material to expand. Because of the offset between the two actuating beams, the axial expansion creates a torque τ around point *P* on the yoke. The torque causes the yoke to rotate the third beam, where the angle of deflection depends on the stiffness of the two actuating beams and the magnitude of the torque. Furthermore, the linear deflection of the yoke depends on the rotation angle and the yoke length.

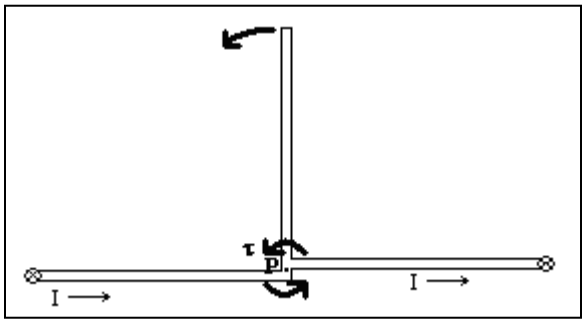

Figure 1. Conceptual actuator design.

The spring constant, k, of the actuator can be modeled as a modified clamped-clamped beam with a moment applied at the center. Assuming that the yoke remains rigid, the clamped-clamped beam can be simplified into two clamped-pinned beams, which act as two springs in parallel. Under actuation, the individual clamped-pinned beam behavior, illustrated in figure 2A, must be modified as the thermal expansion causes the beam to extend around the pinned point with considerations to the length of the offset, as shown in figure 2B. To address this issue, the clamped-pinned beam with over-extension is treated as a standard clamped-pinned beam affixed to a stretching bar.

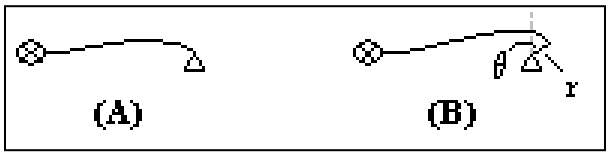

Figure 2. (A) Standard clamped-pinned beam geometry.
(B) Clamped-pinned beam with over-extension geometry.

The torsional spring constant for the rotational actuators is the spring constant of two clamped-pinned beams and two stretching bars all in parallel:

$$k = \frac{8EI}{L_{beam}} + \frac{2EAr^2}{L_{beam}}, \tag{1}$$

in which *E* is Young's modulus, *I* is the moment of inertia, L_{beam} is the length of one actuator beam, *A* is the cross-sectional area of the bar, and *r* is the distance from the axis of the actuator beam to point *P* (*5*).

A curved vernier scale was placed at the end of the deflecting beam to measure the amount of rotation, as shown in figure 3. The rotation angle can be related to the spring constant through a series of conversions that translates the angle of rotation into a force. First, the measured degree of rotation is converted into a linear displacement. The resisting force is extrapolated with the use of the displacement and an opposing beam (or latch) with a known spring constant through Hooke's Law, $F = -kx$, as shown:

$$F = -k_{latch} * L_{yoke} * \sin(\theta_d), \tag{2}$$

in which k_{latch} is the known spring constant of the latch, L_{yoke} is the length of the central yoke, and θ_d is the measured angle of deflection. The spring constant of the latch is found from the equation for a cantilever beam with a transverse load applied at the tip,

$$k_{latch} = \frac{3EI}{L_{latch}^{3}}, \tag{3}$$

in which L_{latch} is the length of the latch (0).

By determining the linear relationship between the actuator output force and the displacement with a given input current, we can determine the linear and torsional spring constant of the actuator can be determined by applying Hooke's law.

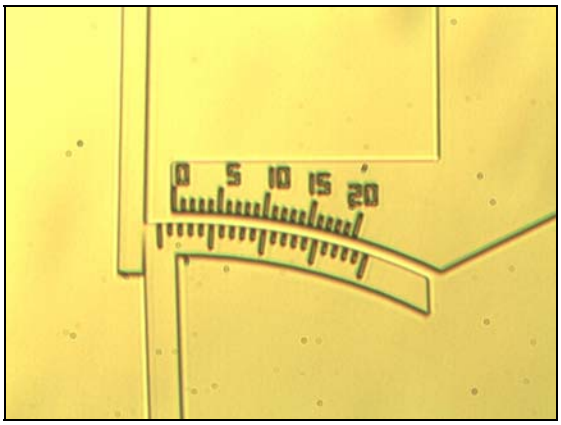

Figure 3. Vernier scale attached to the free beam deflecting against a cantilever latch.

2.2 Fabrication

The rotational actuators were fabricated on silicon-on-insulator (SOI) wafers with a 20-μm device layer, as shown in figure 4A. To form the contact pads, AZ5214 photoresist was patterned to a negative image for lift-off. Spinning and development were performed on a Karl Suss ACS200 photo-lithography cluster tool, and exposure was done with a Karl Suss MA6 mask aligner. After we developed the resist, the wafers were de-scummed in a Metroline M4L plasma processing system to remove any thin residue in the developed features. The metal layers

were deposited with a Carl Herrmann and Associates (CHA) Industries electron beam evaporator, where an adhesion layer of 200 angstrom (Å) of chromium was evaporated onto the wafers, which was immediately followed by the deposition of 4000 Å of gold (figure 4B). The metal layers were then patterned through the lift-off of the resist with J. T. Baker PRS-3000 (figure 4C).

The remaining resist was stripped with acetone, isopropyl alcohol, and deionized water, and a new resist layer was patterned to form the wafer markings and vernier scales. The wafers were etched by deep reactive ion etching (DRIE) for 1 minute to a depth of about 2.5 μm in a Unaxis Versalock (VLR) inductively coupled plasma etcher (figure 4D). The resist was stripped and the wafers were ashed in an oxygen plasma in the Metroline to remove any remaining residue. A new resist layer was spun and patterned to layout the devices (figure 4E). The device-layer silicon was etched by DRIE for 12 minutes until the underlying silicon dioxide layer was exposed (figure 4F). The remaining resist was removed with acetone, isopropyl alcohol, and DI water, and the wafers were ashed in a Metroline (figure 4G). The actuators were then released from the silicon dioxide insulator layer by an isotropic hydrofluoric acid etch in a Primaxx MEMS-clean etch technology (CET) hydro fluoric vapor etcher (figure 4H). Since silicon is infrared-transparent, each wafer was examined under an Idonus transmission infrared microscope to ensure that the underlying oxide had been fully removed from underneath the devices.

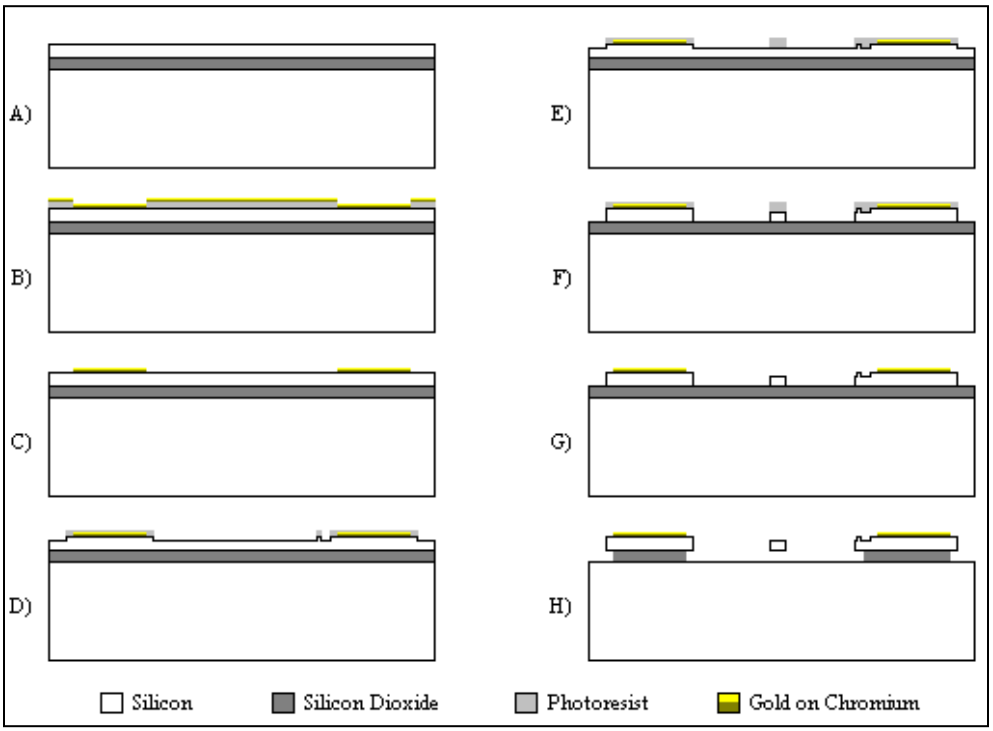

Figure 4. Rotational actuator process sequence.

3. Results and Discussion

The wafers were fabricated with different actuator geometries to characterize the devices and to attempt to determine an optimal actuator configuration. There are variations in the actuating beam length (400/500/600 μm), beam width (5/7/10 μm), and the resisting cantilever latch width (0/10/15/20 μm). The offset from each beam centerline to point *P*, *r*, was kept constant at 5 μm. The beam height was a constant 20 μm, as dictated by the thickness of the SOI wafer used, and the deflecting beam length was kept constant at 485 μm. We performed testing on a probe station by applying a constant current through the actuator via the contact pads of each device. We measured the displacement of the actuators by varying the current and visually observing the changes of the vernier scale under a microscope, as shown in figure 5.

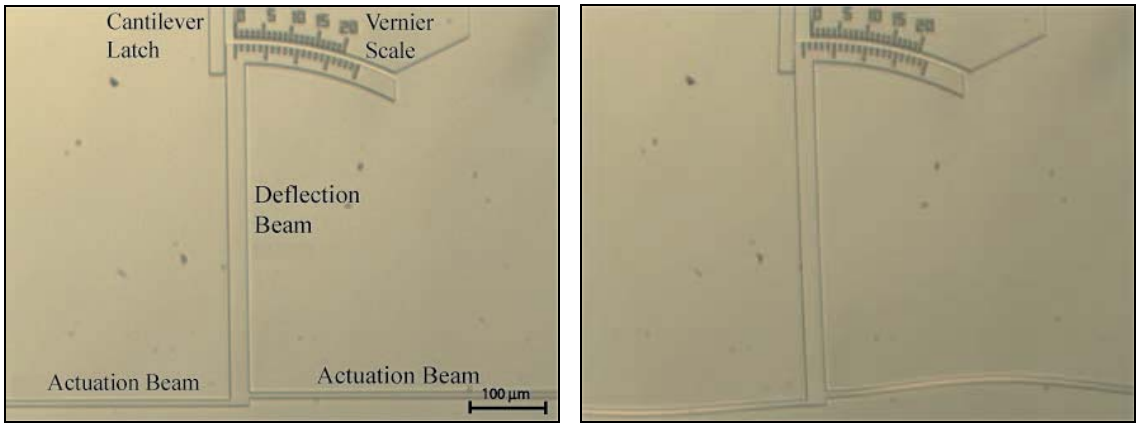

Figure 5. A device (500-μm beam length, 7-μm beam width, and 20-μm resisting cantilever latch width) at rest and under actuation with 29 mA.

The actuators exhibited output forces that were strongly dependent on the width of the actuating beams. Beams with the width of 5 μm were unable to exert enough force to deflect the wider latches through the scope of the vernier from 0 to 1.5º. The activation current was also strongly dependent on the beam width, since wider actuator beams required greater currents to achieve the same deflection. Furthermore, actuating beams with larger lengths required less current to generate displacements similar to the shorter beams. A maximum lateral displacement of 23.7 μm with 0.17 mN of force was measured, and a maximum force of 0.97 mN with a deflection of 17.7 μm was measured.

As previously discussed, the measured angular displacement was translated into generated force. From these values, we determine the spring constant of an actuator by extracting the forces and displacements over different resisting cantilever latch widths for the same beam length, beam width, and current. The linear spring constant for 7-μm-wide, 500-μm-long actuating beams was

determined to be 18.96 N/m, as shown in figure 6A. The respective torsional spring constant of 4.458 μN·m is shown in figure 6B.

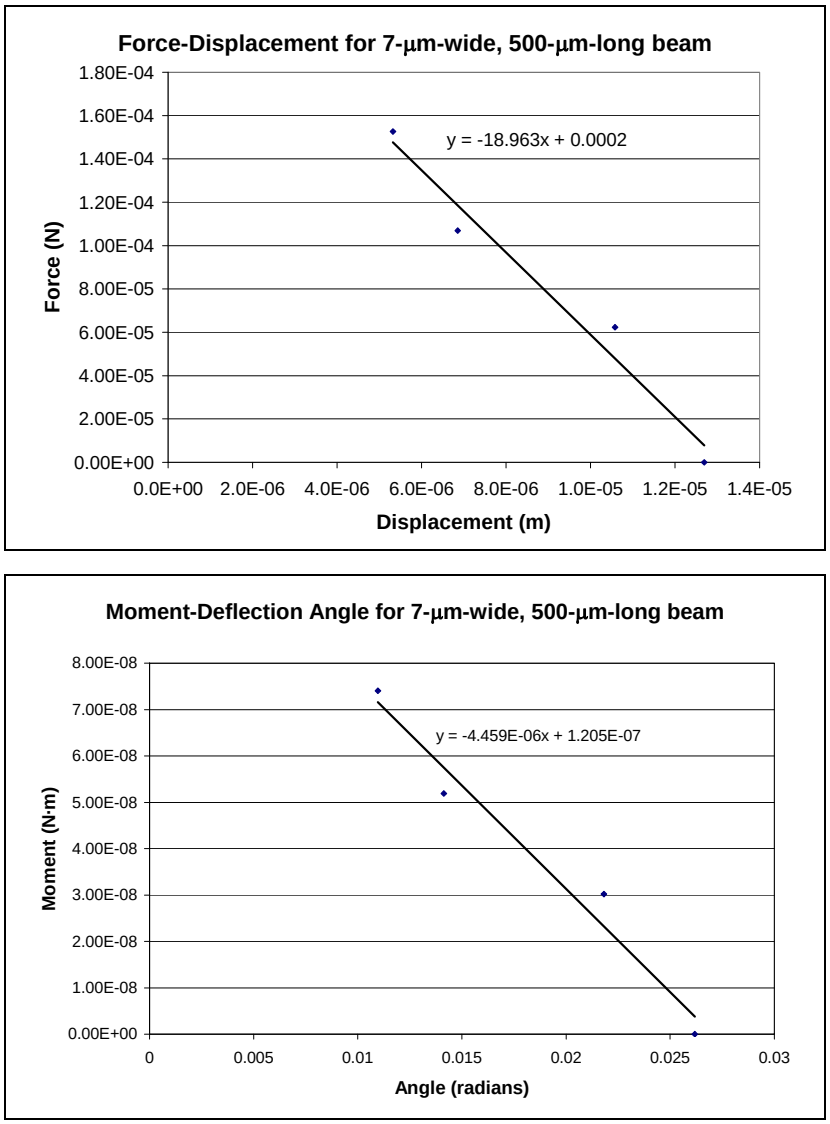

Figure 6. A) Linear and (B) torsional spring constant graphs for a 7-μm-wide, 500-μm-long actuator at 12.9 mA.

The resulting spring constants and their theoretical values for the actuators are shown in table 1.

Table 1. Experimental and theoretical spring constants for various actuators.

Beam Length (μm)	Beam Width (μm)	Current (mA)	Measured Linear Spring Constant (N/m)	Measured Torsional Spring Constant (μN·m)	Theoretical Torsional Spring Constant (μN·m)	Percent Error
400	5	7.7	7.93	3.04	2.82	7.6
	7	11.5	15.80	4.94	4.89	1.0
	10	16.6	24.34	7.33	9.86	–25.6
500	5	8.9	10.34	2.43	2.25	8.0
	7	12.9	18.96	4.46	3.91	14.0
	10	14.6	42.68	10.04	7.89	27.2
600	5	10.4	12.91	1.86	1.88	–0.9
	7	15.2	21.01	3.72	3.26	14.0
	10	22.9	31.19	5.72	6.57	–12.9

The measured torsional spring constants hold some consistency with theory. The predicted values for the 5-μm-wide beams were accurate within 8% error while greater inaccuracies occurred for the 7-μm-wide beams. The measured spring constants for the 10-μm-wide beams were marginal with about 25% error to theory. The resolution of the vernier scales has little effect on the result, since a ±0.1 error in alignment with the gradations only changes the measured spring constant by 0.01 μN·m. It appears that the error is primarily dependent on the beam width and not the beam length, which may be associated with the collinear alignment of wider offset beams resulting in a portion of the axial force being translated into a compressive force on the deflection beam, thereby reducing the effective spring constant.

The maximum deflections for two actuator types, one with a 20-μm-wide latch and one that is free (no latch), are compared to their torsional spring constants in figure 7. The actuators were driven to their maximum currents before device failure (buckling or irreversible plastic beam deformation), and the maximum deflections were measured. The measured and theoretical spring constant decreased with longer beams. The free actuator data showed inconsistency with the expectation that the smaller latch spring constants would result in larger deflections. Comparatively, the spring constant was relatively proportional to the maximum displacement for the actuators with the 20-μm-wide resisting cantilever, with the exception of the 500-μm-long, 10-μm-wide beam, which was shown in table 1 to be an outlier to theory.

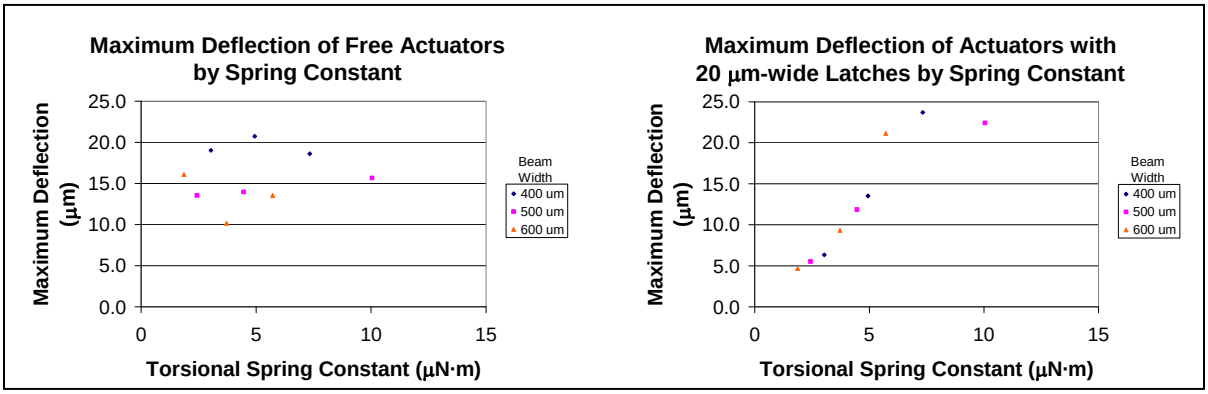

Figure 7. Maximum deflection and spring constant graphs.

By observing the current and voltage required to generate the deflections, we can calculate the power consumption of the devices. The power consumption by displacement for the 400-µm-long beams is shown in figure 8. For the free and 5-µm-wide latch devices, the required power appears to be directly proportional to the displacement. The linearity holds for the actuators with 10-µm-wide beams for all latches; however, the power consumption shows an exponential relationship for the thinner actuating beams with wider latches. This corresponds to the inability of the thinner actuators to generate sufficient force to push stiffer springs through larger deflections.

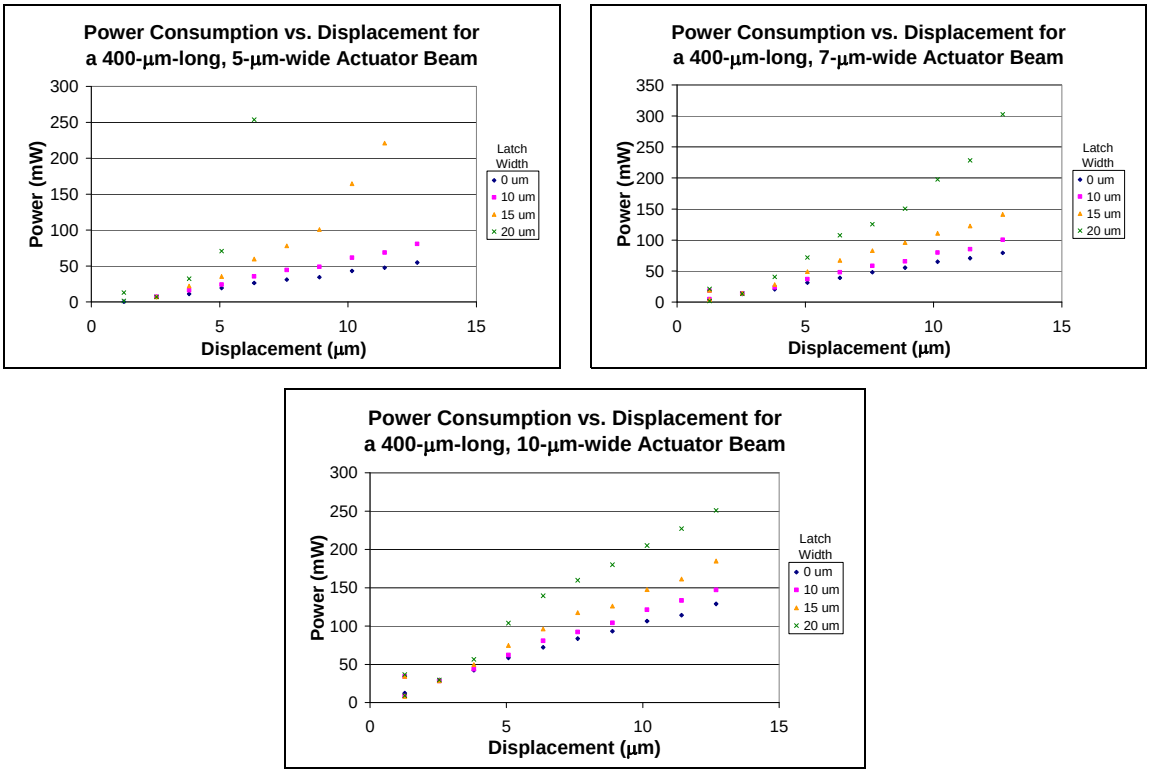

Figure 8. Power consumption-displacement graphs for 400-µm-long beams.

We created a metric for the efficiency of the actuators by comparing the power consumption with the for/ce generated. The results plotted against the actuation displacement are shown in figure 9. It is noted that the power consumption per unit force is plotted on the y-axis; therefore, the lower values are more efficient. Since the short, wide beams require more current, they have a lower efficiency in comparison to the longer and narrower beams. Furthermore, as devices with wider latches are able to generate larger forces, they exhibit greater efficiencies with less than 0.5 mW/μN of power consumption.

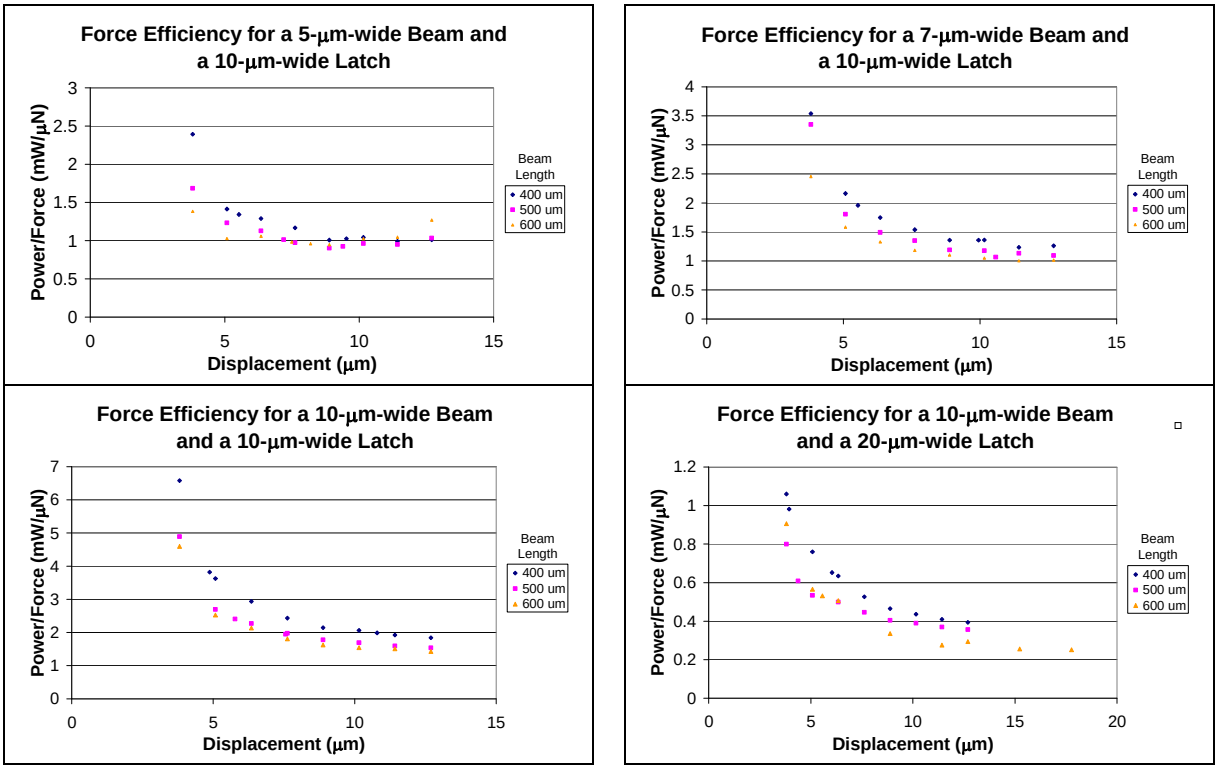

Figure 9. Power consumption-force graphs for various actuators.

The power consumption per unit force tends to approach a minimum, as expected, which corresponds to the maximum deflection. For the 5-μm-wide beam, the efficiency decreases after 10 μm, indicating that the actuators have reached their peak performance, as the beam bending becomes nonlinear and the actuator stiffness decreases. From this point, the actuators cannot continue to generate the force required to deflect the latch farther. For the wider actuator beams, the efficiencies approach a limit, as the minima are not realized.

The peak force efficiencies for various actuator beam dimensions are plotted in figure 10. The best performing actuators were the ones with the widest latches since a relatively larger portion of the generated force is used at the output. Furthermore, the longer actuator beams tended to be more efficient than the shorter beams for constant beam and latch widths. The comparisons of power consumption per unit force for varying beam widths confirmed the trends for matching the force output design with its appropriate application. Ideally, spring constants of beams that

match the spring constants of latches will perform better. Since the thinner latches required smaller forces for deflection, the thinner actuator beams were more appropriate and performed more efficiently than the wider beams. Alternatively, wider latches required a greater force so that the wider actuator beams were more efficient. This holds for the medium 15-μm-wide latch, where the medium 7-μm–wide beam was more efficient than the other two beam widths. The 5-μm-wide, 500-μm-long beam with a 15-μm-wide latch illustrates an efficiency inversion point for the actuators where the power consumption per unit force appeared the same for all lengths.

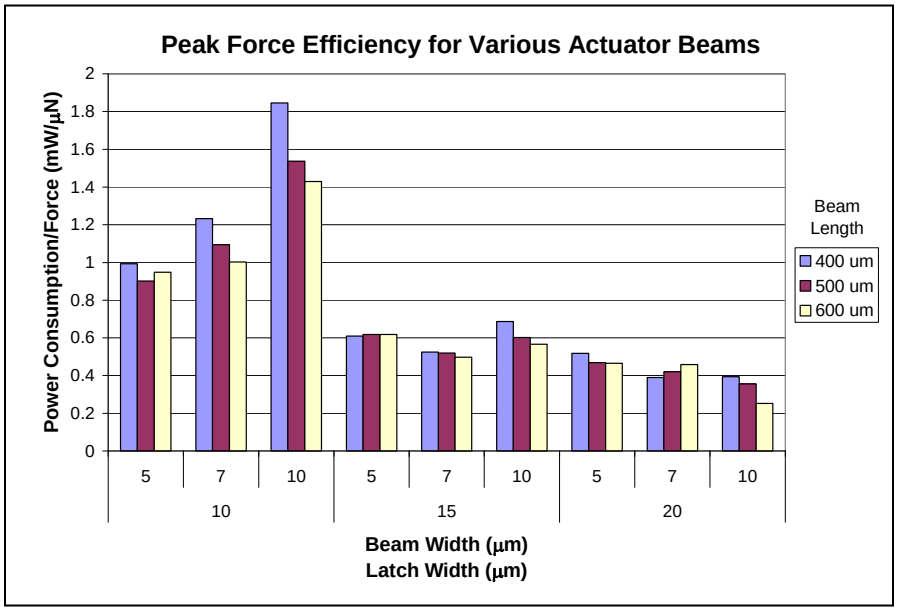

Figure 10. Peak force efficiency over actuator dimensions.

Figure 11 shows the power consumption per unit of maximum displacement for free actuators. Although the 400-μm-long beams exhibited greater peak deflections, the shorter free actuators generally had higher power consumptions per unit deflection. Therefore, the longer actuator beams, which were more efficient in respect to peak forces, were more efficient for maximum deflections as well. Furthermore, the thinner beams consumed less power for maximum deflection, which further supports the previous proposition that the beam efficiency strongly relates to matching the beam spring constant with the latch spring constant, even for an infinitely small latch spring constant. This is consistent with the maximum power theorem, as the optimal power transfer occurs with matched impedances.

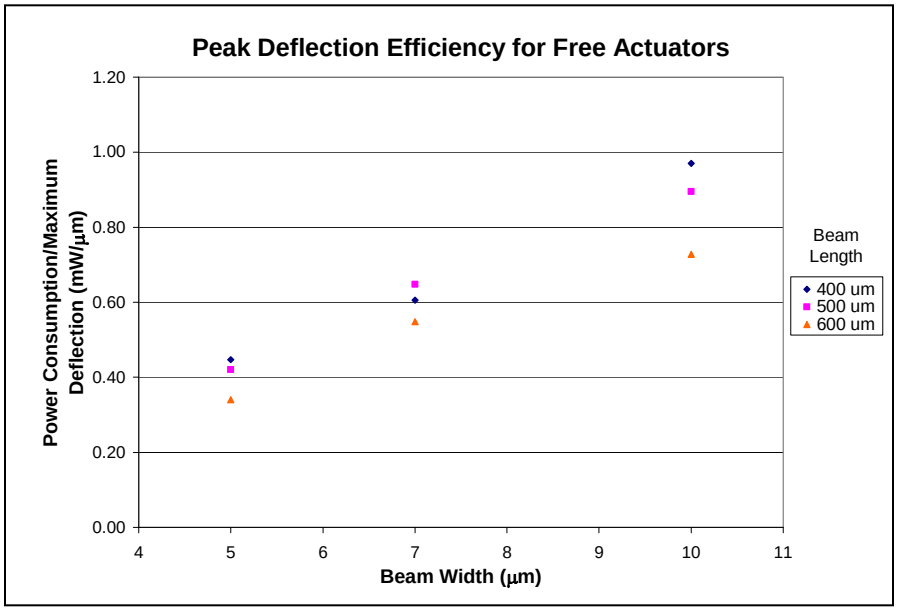

Figure 11. Peak deflection efficiency for free actuators.

4. Conclusions

This project demonstrated a MEMS thermal torsional actuator that was able to efficiently achieve medium forces and displacements. Although the device is intended for rotational actuation, it can be used for linear motion as well. The early testing showed that the actuator can produce 1940 μN/mm^2, requiring an electrical power as low as 0.252 mW/μN. In comparison to other thermal actuators, the preliminary tests show that the rotational actuators are more efficient and provide suitable performance. The bent-beam thermal actuators created by Sinclair had a displacement of ~10 μm at ~3700 μN/mm^2 at 1.53 mW/μN (*6*). The experiment also showed a strong correlation between theoretical spring constants and the measured values for 5-μm beam widths with increasing error with wider actuating beams. To achieve optimum efficiency, it was shown that the spring constant of the actuator should be matched with its appropriate application since there were clear distinctions in performance for maximum force and maximum deflection between the rotational actuator designs.

Future work with the rotational actuators; involves the measurement of velocity and bandwidth and extending the actuators' reliability. The characterization of the actuator velocity and frequency response is necessary for determining further device applications, and long-term, cyclic testing of the actuators will provide a basis for improving the actuator robustness. During testing, issues with undesirable vertical deflections and stiction occurred within two weeks after

the devices were released from the oxide. Failure analysis of the actuators should lead to improvements in the device design without compromising the current performance. Finally, there is an effort to fabricate an in-plane piezoelectric rotational actuator made with lead zirconate titanate, which should further improve the efficiency.

5. References

1. Que, L.; Park, J.; Gianchandani, Y. Bent-Beam Electro-Thermal Actuators for High Force Applications. *IEEE International Conference on Micro Electro Mechanical Systems*, Orlando, Florida, Jan. 1999, 552–7.

2. Lee, T.; Seo, Y.; Whang, K.; Choi, D. Study on the Lateral Actuator with Actuation Range Amplifying Structure. *Key Engineering Materials* **2006**, (*326–328*) 289–292.

3. Trolier-McKinstry, S.; Muralt, P. This Film Piezoelectrics for MEMS. *Journal of Electroceramics* **2004**, *12*, 7–17.

4 Currano, L. Analysis of a Clamped-Clamped-Free Three-Bar Structur", U. of MD Term Paper, May 2006.

5. Blevins, R. D. *Formulas for Natural Frequency and Mode Shape*, Krieger, 40-47, 1984.

6. Sinclair, M. A High Force Low Area MEMS Thermal Actuator. *2000 Inter Society Conference on Thermal Phenomena* **2000**, 127-32.

INTENTIONALLY LEFT BLANK

Distribution List

ADMNSTR
DEFNS TECHL INFO CTR
ATTN DTIC-OCP (ELECTRONIC COPY)
8725 JOHN J KINGMAN RD STE 0944
FT BELVOIR VA 22060-6218

DARPA
ATTN MTO A LAL
ATTN MTO D POLLA
3701 N FAIRFAX DR
ARLINGTON VA 22203-1714

US ARMY CECOM, INTLLGNC & INFO WARFARE DIRCTRT
SIGINT & PAYLOAD INTGRTD DIV
INTLGNC COLLECT BR
ATTN AMSEL-RD-IW-SC
E POTENZIANI II
RM 150 BLDG 600 MCAFEE CENTER
FT MONMOUTH NJ 07703-5211

US ARMY AMRDEC
ATTN AMSAM-RD-WS-IL T HUDSON
BLDG 7804
REDSTONE ARSENAL AL 35898

US ARMY ARDEC
ATTN AMSTA-AR-TA
BLDG 1
PICATINNY ARSENAL NJ 07806-5000

US ARMY RSRCH LAB
ATTN AMSRD-ARL-CI-OK-TP TECHL LIB T LANDFRIED
BLDG 4600
ABERDEEN PROVING GROUND MD 21005-5066

NAVAL SURFACE WARFARE CENTER
INDIAN HEAD DIVISION WEAPONS DEPT
ATTN D JEAN
101 STRAUSS AVE
INDIAN HEAD MD 20640

US GOVERNMENT PRINT OFF
DEPOSITORY RECEIVING SECTION
ATTN MAIL STOP IDAD J TATE
732 NORTH CAPITOL ST., NW
WASHINGTON DC 20402

DIRECTOR
US ARMY RSRCH LAB
ATTN AMSRD-ARL-RO-EV W D BACH
PO BOX 12211
RESEARCH TRIANGLE PARK NC 27709

US ARMY RSRCH LAB
ATTN AMSRD-AAR-AEP-F(A)
C ROBINSON
ATTN AMSRD-AAR-AEP-F (A)
G SMITH
ATTN AMSRD-ARL-CI-OK-T TECHL PUB (2 COPIES)
ATTN AMSRD-ARL-CI-OK-TL TECHL LIB (2 COPIES)
ATTN AMSRD-ARL-D J M MILLER
ATTN AMSRD-ARL-SE J PELLEGRINO
ATTN AMSRD-ARL-SE-R
P AMIRTHARAJ
ATTN AMSRD-ARL-SE-RL D GEE (3 COPIES)
ATTN AMSRD-ARL-SE-RL
J COSTANZA

US ARMY RSRCH LAB (cont'd)
ATTN AMSRD-ARL-SE-RL
L CURRANO (3 COPIES)
ATTN AMSRD-ARL-SE-RL M DUBEY
ATTN IMNE-ALC-IMS MAIL & RECORDS MGMT
ADELPHI MD 20783-1197